Technical Paper 1624

Wear Particles of Single-Crystal Silicon Carbide in Vacuum

Kazuhisa Miyoshi and Donald H. Buckley

FEBRUARY 1980

NASA

NASA Technical Paper 1624

Wear Particles of Single-Crystal Silicon Carbide in Vacuum

Kazuhisa Miyoshi and Donald H. Buckley
Lewis Research Center
Cleveland, Ohio

Summary

An investigation was conducted to examine the nature of fracture of silicon carbide and particle formation in wear. Sliding friction experiments were conducted with the single-crystal silicon carbide {0001} surface sliding in the $\langle 10\overline{1}0 \rangle$ direction in contact with various iron-based binary alloys. Experiments were conducted with a load of 0.2 N, at a sliding velocity of 3×10^{-3} meter per minute in a vacuum of 10^{-8} pascal at room temperature.

The results of the investigation indicate that multiangular and spherical wear particles of silicon carbide are observed as a result of multipass sliding. The multiangular wear particles are produced by primary and secondary cracking of cleavage planes {0001}, {10$\overline{1}$0}, or {11$\overline{2}$0} under the Hertzian stress field or local inelastic deformation zone at the interface. The spherical wear particles of silicon carbide may be produced by two mechanisms: (1) a penny-shaped fracture along the circular stress trajectories under the local inelastic deformation zone, and (2) attrition of wear particles.

Introduction

Silicon carbide is expected to be one of the most desirable materials from various aspects for use in high-hardness and/or temperature applications such as turbine blades, vanes and shrouds in gas turbine engines, ceramic seals, stable high-temperature semiconductors, first wall materials in a controlled thermonuclear reactors, and as abrasives for metal removal.

The present authors have conducted experimental work to determine the tribological properties of single-crystal silicon carbide (refs. 1 and 2). Wear particle characteristics, such as particle shape, composition, size distribution, quantitative levels, physical and chemical properties, are sufficiently able to qualify and specify the tribological behavior such as wear behavior, mode, and mechanism.

Platelets of hexagonal silicon carbide wear debris have been observed by the present authors with the formation of platelets, as a result of silicon carbide sliding against itself and pure metals (refs. 1 and 2). Such wear particles, having crystallographically oriented sharp edges, indicated that fracture wear of silicon carbide was due to cleavage of both prismatic and basal plane.

Hexagonal and rectangular platelet wear debris are also observed with manganese-zinc ferrite surfaces as a result of sliding contact with itself and pure metals (refs. 3 and 4). The experimental evidence showed the fracture wear of manganese-zinc ferrite is due to cleavage of {110} planes.

Coefficients of friction for iron-based binary alloys (alloying elements were Ti, Cr, Mn, Ni, Rh, and W) sliding against silicon carbide are generally twice as large (or more) as those observed for pure metals or for silicon carbide sliding against silicon carbide (refs. 5 and 6). It is of interest to develop an understanding of the fracture behavior and wear particle generation of silicon carbide, such as under high adhesion conditions in sliding contact with various alloys.

Another matter of interest is knowing whether any other types of silicon carbide wear particle, such as spherical wear particles, can be generated under conditions of high adhesion and friction.

The objective of the present paper is to examine the nature of fracture of silicon carbide and wear particles relative to fracture wear. Friction experiments were conducted with the single-crystal silicon carbide {0001} surface sliding in the $\langle 10\overline{1}0 \rangle$ direction in contact with various iron-based binary alloys. All experiments were conducted with a load of 0.2 newton, at a sliding velocity of 3×10^{-3} meter per minute with a total sliding distance of 2.5 millimeters in single-pass sliding, in a vacuum of 10^{-8} pascal at room temperature. When alloy surfaces are in contact with silicon carbide under a load of 0.2 newton, the alloy around the contact area is subjected to stresses that are close to the elastic limit in elastic deformation region and/or exceed it.

Materials

The single-crystal silicon carbide used in these experiments was a 99.9-percent-pure compound of silicon and carbon and had a hexagon-closed packed crystal structure. The composition data and hardness of single-crystal silicon carbide are presented in table I. The Knoop hardness was 2954 in the $\langle 10\overline{1}0 \rangle$ direction and 2917 in the $\langle 11\overline{2}0 \rangle$ direction on the basal {0001} plane of silicon carbide (ref. 7).

Table II presents the analyzed compositions in atomic percent and Vickers hardness of iron-base alloys, which are used in this investigation and prepared by Stephens and Witzke (ref. 8). The iron-

base binary alloys of reference 8 were prepared by arc-melting the high-purity iron and high-purity alloying elements (Ti, Cr, Mn, Ni, Rh, and W). The solute concentrations ranged from approximately 0.5 atomic percent for those elements that have extremely limited solubility in iron up to approximately 16 atomic percent for those elements that form a continuous series of solid solutions with iron.

Experimental Apparatus and Procedure

Apparatus

The apparatus used in this investigation is shown schematically in figure 1 and is described in reference 2.

Specimen Preparation

The disk flats of silicon carbide and the iron-base binary alloy pin specimens were polished with 3-micrometer-diameter diamond powder and then 1-micrometer aluminum oxide (Al_2O_3) powder. The radius of the pins was 0.79 millimeter. The pin and disk surfaces were rinsed with 200 proof ethyl alcohol.

Experimental Procedure

The specimens were placed in the vacuum chamber, and the chamber was evacuated and subsequently baked out to obtain a pressure of 1.33×10^{-8} pascal (10^{-10} torr). When this pressure was obtained, argon gas was bled back into the vacuum chamber to a pressure of 1.3 pascal. A -1000-volt-direct-current potential was applied to the specimens, and the specimens (both disks and pins) were argon sputter bombarded for 30 minutes. One hour after the sputtering operation was completed the vacuum chamber was reevacuated, and AES (Auger emission spectroscopy) spectra of the disk surface were obtained to determine the degree of surface cleanliness. When the desired degree of cleanliness of disk was achieved, friction experiments were conducted.

A load of 0.2 newton was applied to the pin-disk contact by deflecting the beam of figure 1. Both load and friction force were continuously monitored during a friction experiment. Sliding velocity was 3 millimeters per minute, with a total sliding distance of 2.5 millimeters in single pass sliding. All friction experiments in vacuum were conducted with the system evacuated to a pressure of 10^{-8} pascal.

Results and Discussion

Cleanliness of Silicon Carbide Surfaces

An Auger emission spectroscopy spectrum of the single-crystal silicon carbide {0001} surface was obtained before sputter cleaning. The crystal was in the as-received state other than having been baked out in the vacuum system. In addition to the silicon and carbon peaks, an oxygen peak was observed. The oxygen peak and chemically shifted silicon peaks at 78 and 89 electron volts (eV) indicated a layer of SiO_2 on the silicon carbide surfaces as well as a simple adsorbed film of oxygen (refs. 9 and 10). The Auger spectrum taken after the silicon carbide surface had been sputter cleaned clearly revealed the silicon and carbon peaks at 92 and 272 eV, respectively. The oxygen peak was negligible.

Friction Behavior

Multipass sliding friction experiments were conducted with iron-base binary alloys with various concentrations of solute alloyed in iron in contact with single-crystal silicon carbide in vacuum. The binary alloy systems were iron alloyed with titanium, chromium, manganese, nickel, rhodium, or tungsten. The tribological behavior of these materials has already been discussed in references 6 and 11. Briefly, the friction-force traces obtained in this investigation are generally characterized by a sharp break in the friction-force, that is, stick-slip behavior. The coefficients of friction for alloys, having high solute concentration (see example in fig. 2(a)) or chemically active alloying elements (Mn, Ni, W, and Ti) generally decreased with the number of passes, when repeated passes of the alloy riders were made over the same single-crystal silicon carbide surface. The coefficient of friction for first pass sliding differed from those for the second and multiple pass sliding. This difference was due to a large amount of alloy transfer that took place to the silicon carbide surface in the first, single-pass of the rider. On the other hand, the coefficients of friction for the alloy, having low solute concentration (see fig. 2(b)) or chemically less active alloying elements (e.g., Rh) were generally small changes and fluctuated with the number of passes.

Fracture Wear

The sliding of an alloy rider on a silicon carbide surface results in the formation of cracks and fracture pits in the near contact region of the silicon carbide surface as well as that on the metal rider (refs. 1

and 2). Figure 3 presents scanning electron micrographs of the wear tracks on silicon carbide surfaces, where the wear tracks were generated by 10-pass sliding of 8.06 atomic percent rhodium-iron alloy and 6.66 atomic percent tungsten-iron alloy riders, respectively. The wear tracks are accompanied by microfracture pits. Silicon carbide wear debris has already been ejected from the wear track in figure 3(a), but a particle of wear debris is still partially in the microfracture pit in figure 3(b). Such microfracture pits and wear debris have generally crystallographically oriented sharp edges generated by surface crackings along $\{10\bar{1}0\}$ or $\{11\bar{2}0\}$ planes. The bottom surfaces of the fracture pits are generally very smooth. This is due to the subsurface cleavage along $\{0001\}$ planes, which are parallel to the sliding interface.

Figure 4 presents a scanning electron micrograph of a wear track on a silicon carbide surface accompanied by an exceptionally large fracture pit. A large light area at the beginning of wear track is a fracture pit where the wear track was generated by 10-pass sliding of a 8.12 atomic percent titanium-iron alloy rider across the surface. Most of the silicon carbide wear debris has already been ejected from the wear track. The smooth surface at the bottom of the fracture pit is due to subsurface cleavage along $\{0001\}$ planes.

Figure 5 presents a scanning electron micrograph and an X-ray map of a wear scar of a 8.12 percent titanium-iron alloy rider after it slid against the silicon carbide surface already shown in figure 4. The wear scar contains a large amount of silicon carbide wear debris which was produced in multipass sliding of the alloy rider and was embedded in the alloy rider. The concentration of white spots in figure 5(b) correspond to silicon carbide wear debris locations in figure 5(a) where silicon carbide transfer is evident. Figure 6 is a scanning electron micrograph at the beginning of the wear scar examined at high magnification (see the small rectangle in fig. 5(a)). Again, the copious amount of silicon carbide wear debris, having crystallographically oriented sharp edges, was seen on the wear scar of the alloy rider. The subject of the wear debris particle will be discussed in more detail in succeeding sections.

Multiangular Wear Debris

Figure 7 illustrates detailed examination of silicon carbide wear debris produced by 10-pass sliding of riders on the silicon carbide surfaces. The scanning electron micrographs clearly reveal evidences of various multiangular wear debris particles of silicon carbide, which transferred to the 1.02 atomic percent Ti-Fe alloy rider (fig. 7(a)). Wear debris was observed near the silicon carbide wear track when sliding against the 3.86 atomic percent Ti-Fe alloy rider (fig. 7(b)). Such multiangular wear debris particles have crystallographically oriented sharp edges and are nearly a rhombus, parallelogram, or square in shape. These shapes may be related to surface and subsurface cleavage of $\{10\bar{1}0\}$, $\{11\bar{2}0\}$, and $\{0001\}$ planes. This formation of wear debris is consistent with earlier studies for silicon carbide in sliding contact with metals and itself (refs. 1 and 2). The authors have already observed the hexagonal fracture pit of silicon carbide and the formation of platelet hexagonal wear debris. These shapes were observed to occur as a result of sliding of single-crystal silicon carbide on itself in reference 1. It was also observed for metals in contact with silicon carbide that the crystallographically oriented cracking and fracturing of silicon carbide occurred near the adhesive bond to the metal (ref. 2).

Similar multiangular wear debris particles, having crystallographically oriented sharp edges, were also observed with manganese-zinc ferrite in sliding contact with pure metals and manganese-zinc ferrite in vacuum (refs. 3 and 4).

Spherical Wear Debris

It is understandable that the fracturing of ceramic materials and the formation of wear debris may be characterized by crystallographic orientation as demonstrated in the former sections. However, more detailed examination of the wear track on the silicon carbide and the wear scar on the alloy riders revealed in addition evidence of spherical wear particles of silicon carbide. Figures 8(a) and (b) show a scanning electron micrograph and an X-ray dispersive analysis map of a nearly spherical wear particle and a groove, produced in a plastic manner by the plowing action of the particle. This dislodged spherical wear particle could be observed near the wear scar of the 1.02 atomic percent titanium-iron alloy rider after 10-passes of sliding on the silicon carbide surface.

Figure 9 consists of scanning electron micrographs of rider wear scars after sliding against a silicon carbide surface. These figures reveal spherical indentations and straight grooves along the sliding direction on the rider surfaces formed by indenting and plowing the spherical wear debris. Such a spherical wear particle and its indentation and groove were primarily observed for the alloys with low solute concentrations presented in table II. These results reveal that (1) a nearly spherical wear particle can be produced by sliding friction, (2) the wear particle plows the surface of the alloy rider during sliding, that is, the hardness of the particle is much greater than that of the alloy rider surface, and (3) the wear particle includes the element of silicon, as shown by the X-ray map of Si K_α. The next question is what is the real

3

wear debris particle, since the wear particle includes the element silicon.

Figure 10 shows partially spherical wear debris particles observed on the silicon carbide surfaces in sliding contact with the 1.02 atomic percent titanium-iron alloy rider. The nearly spherical particles are very similar to the particle observed on the wear scar shown in figure 8. The partially spherical wear particles include a multiangular and a spherical portion. Partially spherical wear particles were also observed with the multiangular wear debris particles on the wear scar of the alloy, as shown in figure 11.

Figure 12 presents brittle fractured wear particles observed near the wear tracks of silicon carbide surfaces. The wear particles contain both sharp edges and round portions. The formation of sharp edges may be related to cleavage cracking in the formation of wear debris. The round portion would indicate that the particles had been nearly or partially spherical before fracturing. These figures also indicate that the wear debris particles are characterized by having the feature of being hollow. The outer and inner circles of the particles seem to be concentric. Thus, the formation of partially spherical wear particle and the brittle fracture of the particle indicates that the spherical wear particle is silicon carbide, because of detection of Si K_{α} X-ray map from the particles and the brittleness of the particles.

It is well known that the spherical wear particles of metals are generated in rolling contact fatigue and that these are associated with bearing fatigue cracks (refs. 12 to 17). The evidence of this investigation, however, clearly reveals that the rolling bearing contact is not the only generation source of spherical wear particles. Multipass sliding with high adhesion may also be a generation source of spherical wear particles for the brittle material.

Fracture Mechanisms

As indicated in the previous sections, sliding of the spherical alloy rider may produce fracture wear of silicon carbide, and subsequently generate multiangular and spherical wear particles of silicon carbide. Let us consider the fracture mechanisms of silicon carbide in the two sliding processes reported herein:

(1) First single-pass sliding. The applied forces in this investigation contain both normal and tangential components, the latter of which can arise from oblique loading and interfacial friction between rider and disk specimens.

The fracture of single-crystal silicon carbide may occur in the following processes, which are schematically shown in figure 13. First, the alloy around the tip of the rider is deformed well beyond the elastic limit and is deformed plastically (fig.

13(a)). The mean contact pressure over the deformed area approaches the hardness of the alloy. The counterface of the flat silicon carbide is subjected to point-contact loading with a flat circle of radius a_o. It is deformed elastically because the hardness of silicon carbide is 10 to 50 times greater than the hardness of alloys examined in this investigation. If the flat were an isotropic material, the stress trajectories in the contact of figure 13(a) would produce a Hertzian stress field in the flat specimen (ref. 18). Although the influence of the crystallographic orientation must be imposed on the stress field in this investigation, the stress trajectories may be similar to the Hertzian field (ref. 19). The cracking will suddenly initiate at a pre-existing flow, almost certainly at the surface just outside the contact circle where the contours of greatest principle tensile stress exist during loading.

In figure 13(b), in addition to an increase in load, friction force causes a junction growth at the interface, and subsequently promotes the stable growth of the initial cracks along the primary cleavage planes of silicon carbide $\{0001\}$, $\{10\bar{1}0\}$, and $\{11\bar{2}0\}$, this will further generate new small cracks in the same manner, as mentioned in the discussion of figure 13(a). Note that if the disk were in isotropic material, the Hertzian surface ring crack propagation downward occurs at the circular stress trajectories in the Hertzian elastic field, and subsequently a Hertzian (truncated) cone may be formed (ref. 20).

In figure 13(c), an increase in friction force causes, further, junction growth and stable growth of the initial cracks. The cracks (called primary cracks) have grown straight downward and the tip of crack subsurface becomes curved and propagates along a secondary weak plane, that is, another primary cleavage plane. For example, when the sliding surface of silicon carbide is the basal plane, the secondary cracks propagate parallel to the sliding surface, that is, to the basal plane (ref. 21).

In figure 13(d), rider sliding, which contains both loading and unloading of normal load and friction force, causes the stable growth of secondary cracks and the intersecting of primary and secondary cracks.

In figure 13(e), removal of fractured wear debris occurs as a result of stress relaxation in unloading. Again, for the single-crystal silicon carbide the primary and secondary cracks may generate and propagate along the cleavage planes $\{0001\}$, $\{10\bar{1}0\}$ or $\{11\bar{2}0\}$, and then they intersect each other. The multiangular fracture pits and multiangular wear debris of silicon carbide shown in figures 3, 4, 6, 7, and references 1 and 2 may be generated by the aforementioned fracture mechanisms.

(2) Multipass sliding. The surfaces of pin and disk specimens include alloy wear, wear debris of alloy and silicon carbide, fracture pits and cracks as a

4

result of the first single-pass sliding. The friction and wear behavior during multipass sliding on the same wear track may be strongly influenced by the surface conditions generated in the first pass. The multipass sliding involves repeated loading cycles of the normal load and friction force. A discussion, therefore, of the fracture behavior in multipass sliding must be considered from two aspects: (1) stress concentration and (2) fatigue and attrition of particles formed.

Stress concentration aspect. — The wear debris of the alloy and silicon carbide, which transferred to the counter surfaces or was dislodged, and fracture pits in the wear track can produce local stress concentration at the interface. The sources of stress concentration are schematically shown in figure 14. There are small silicon carbide and alloy wear particles and/or fracture pits at the interface. The stress concentration at the sharp edges of wear debris or fracture pits may produce a small zone of inelastic deformation in silicon carbide about the sharp edge. Cracks will subsequently be initiated in the two possible favored geometries, as shown in figures 15 and 16 (ref. 22). Figure 15 indicates that (1) the sharp point produces a plastic deformation region, (2) a deformation-induced flow or crack already produced in the first pass of sliding develops into a crack or stable growth of a crack subsurface from the inelastic deformation zone, (3) on unloading or application of sliding friction force the crack closes or expands and secondary cracks begin to develop, and (4) the cracks grow steadily below the subsurface. Such fracture may produce the multiangular silicon carbide wear particle during multipass sliding.

Figure 16 indicates another possible cracking mechanism, that is, sudden development of a penny-shaped crack along the circular stress trajectories. It is known that the penny-shaped crack is produced in amorphous materials such as soda-lime glass under Vickers indentation (ref. 22). The influence of crystallinity, however, is imposed on the crack geometries of anisotropic materials such as silicon carbide, and accordingly the crack geometry is observed. Therefore, the penny-shaped cracks may not be a circle in silicon carbide. But the possibility of a fracture such as the one shown in figure 16, that is, a nearly circular or spherical fracture, would still exist in a single crystal because it is possible that the cracks would grow and pile up in atomistic terms by the sequential rupture of cohesive bonds along the circular stress trajectories shown in figure 16. Thus, this fracture mechanism may explain the possibility of generating a spherical wear particle.

Fatigue or attrition action aspect. — The repeated number of sliding passes, which include repeated loading and unloading of the normal load and friction force, produce a stressing and unstressing field in the material, and subsequently generate cracks such as those schematically shown in figures 13, 15, and 16. The surface fatigue wear may be of great importance in the formation of cracks and fractured wear debris in multipass sliding.

Edges of wear particles such as multiangular or irregular particles undergo attrition by chipping during multipass sliding. The fragmentation of the silicon carbide wear particle developed by the attrition of wear particles may be another possibility for generating spherical wear particles.

Conclusions

As a result of sliding friction experiments conducted in this investigation with single-crystal silicon carbide in sliding contact with iron-base binary alloys in high vacuum, the following conclusions are drawn:

1. Multiangular and spherical wear particles of silicon carbide are observed as a result of multipass sliding.

2. Multiangular wear particles are produced by primary and secondary cracking of cleavage planes $\{0001\}$, $\{10\overline{1}0\}$ or $\{11\overline{2}0\}$ under the Hertzian stress field or local inelastic deformation zone in the interface.

3. Spherical wear particles of silicon carbide may be produced by two mechanisms: a penny-shaped fracture along the circular stress trajectories under local inelastic deformation zone and the attrition and fatigue of wear particles.

Lewis Research Center,
  National Aeronautics and Space Administration,
    Cleveland, Ohio, October 10, 1979,
      506-16.

References

1. Miyoshi, Kazuhisa; and Buckley, Donald H.: Friction and Fracture of Single-Crystal Silicon Carbide in Contact with Itself and Titanium. ASLE Trans., vol 22, no. 2, Apr. 1979, pp. 146-153.
2. Miyoshi, Kazuhisa; and Buckley, Donald H.: Friction and Wear Behavior of Single-Crystal Silicon Carbide in Sliding Contact with Various Metals. ASLE Trans., vol. 22, no. 3, Jul. 1979, pp. 245-256.
3. Miyoshi, Kazuhisa; and Buckley, Donald H.: Anisotropic Friction and Wear of Single-Crystal Manganese-Zinc Ferrite in Contact with Itself. NASA TP-1339, 1978.
4. Miyoshi, Kazuhisa; and Buckley, Donald H.: Friction and Wear of Single-Crystal and Polycrystalline Manganese-Zinc Ferrite in Contact with Various Metals. NASA TP-1059, 1977.
5. Miyoshi, Kazuhisa; and Buckley, Donald H.: Friction and Wear Characteristics of Iron-Chromium Alloys in Contact with Themselves and Silicon Carbide. NASA TP-1387, 1979.

6. Miyoshi, Kazuhisa; and Buckley, Donald H.: Adhesion, and Friction of Iron-Base Binary Alloys in Sliding Contact with Silicon Carbide in Vacuum. NASA TP-1604, 1979.

7. Shaffer, Peter T. B.: Effect of Crystal Orientation on Hardness of Silicon Carbide. J. Am. Ceram. Soc., vol. 47, no. 9, Sep. 1964, p. 466.

8. Stephens, Joseph R.; and Witzke, Walter R.: Alloy Softening in Binary Iron Solid Solutions. J. Less-Common Metals, vol. 48, Aug. 1976, pp. 285-308.

9. Johannesson, J. S.; Spicer, W. E.; and Strausser, Y. E.: An Auger Analysis of the SiO_2-Si Interface. J. Appl. Phys., vol. 47, no. 7, July 1976, pp. 3028-3037.

10. Miyoshi, Kazuhisa; and Buckley, Donald H.: Effect of Oxygen and Nitrogen Interactions on Friction of Single-Crystal Silicon Carbide. NASA TP-1265, 1978.

11. Miyoshi, Kazuhisa; and Buckley, Donald H.: Friction and Wear of Iron-Base Binary Alloys in Sliding Contact with Silicon Carbide in Vacuum. NASA TP-1612, 1980.

12. Scott, D., and Mills, G. H.: Spherical Debris - Its Occurrence, Formation and Significance in Rolling Contact Fatigue. Wear, 24, May 1973, pp. 235-242.

13. Scott, D.; Seifert, W. W.; and Westcott, V. C.: The Particles of Wear. Sci. Am., vol. 230, no. 5, May 1974, pp. 88-97.

14. Middleton, J. L.; Westcott, V. C.; and Wright, R. W.: The Number of Spherical Particles Emitted by Propagating Fatigue Cracks in Rolling Bearings. Wear, vol. 30, Nov. 1974, pp. 275-277.

15. Scott, D.: Debris Examination - A Prognostic Approach to Failure Prevention. Wear, vol. 34, Aug. 1975, pp. 15-22.

16. E. Roderic Bowen, and Vernon C. Westcott: Wear Particle Atlas. Naval Air Engineering Center, July 1976.

17. Loy, B.; and McCallum, R.: Mode of Formation of Spherical Particles in Rolling Contact Fatigue. Wear, vol. 24, 1973, pp. 219-228.

18. Hertz, H.: Ueber die Beruhrung Fester Elastischer Korper. J. Reine Angew. Math., vol. 92, 1881, pp. 156-171.

19. Lawn, B. R.: Hertzian Fracture in Single Crystals with the Diamond Structure. J. Appl. Phys., 39 no. 10, Sep. 1968, pp. 4828-4836.

20. Mikosza, A. G. and Lawn, B. R.: Section and Etch Study of Hertzian Fracture Mechanics. J. Appl. Phys. vol. 42, no. 13, Dec. 1971, pp. 5540-5545.

21. Miyoshi, K.; and Buckley, D. H.: Friction, Deformation and Fracture of Single-Crystal Silicon Carbide, ASLE Trans., vol. 22, no. 1, Jan. 1979, pp. 79-90.

22. Lawn, B. R. and Swain, M. V.: Microfracture Beneath Point Indentations in Brittle Solids. J. Mater. Sci., vol. 10, no. 1, Jan. 1975, pp. 113-122.

23. Taylor, A.; and Laidler, D. S.: The Formation and Crystal Structure of Silicon Carbide. Brit. J. Appl. Phys., vol. 7, July 1950, pp. 174-181.

24. Shaffer, P. T. B.: A Review of the Structure of Silicon Carbide. Acta Crystallogr., Sect. B, vol. 25, 1969, pp. 477-488.

TABLE II. - CHEMICAL ANALYSIS, SOLUTE/IRON

ATOMIC RADIUS RATIO, AND HARDNESS DATA

FOR BINARY IRON ALLOYS (REF. 8)

Solute element	Analyzed solute content, at %	Analyzed interstitial content, ppm by weight			Solute/iron atomic radius ratios	Vickers hardness number at 300 K
		C	O	P		
Ti	1.02	56	92	7	1.1476	93
	2.08	--	--	--	→	117
	3.86	87	94	9		152
	8.12	--	--	--		286
Cr	0.99	--	--	--	1.0063	57
	1.98	50	30	12	→	67
	3.92	--	--	--		66
	7.77	40	85	10		82
	16.2	--	--	--		111
Mn	0.49	--	--	--	0.9434	61
	.96	39	65	6	→	75
	1.96	--	--	--		87
	3.93	32	134	8		140
	7.59	--	--	--		209
Ni	0.51	--	--	--	0.9780	66
	1.03	28	90	6	→	75
	2.10	--	--	--		91
	4.02	48	24	5		112
	8.02	--	--	--		160
	15.7	38	49	7		228
Rh	1.31	--	--	--	1.0557	90
	2.01	20	175	22	→	103
	4.18	--	--	--		123
	8.06	12	133	19		159
W	0.83	30	140	12	1.1052	102
	1.32	--	--	--	→	122
	3.46	23	61	21		152
	6.66	--	--	--		190

TABLE I. - COMPOSITION DATA, CRYSTAL STRUCTURE, AND

HARDNESS OF SINGLE-CRYSTAL SILICON CARBIDE

(a) Composition[a]

Si	C	O	B	P	Others
66.6%	33.3%	<500 ppm	<100 ppm	<200 ppm	<0.1 ppm

(b) Crystal structure and hardness

Crystal structure	Interatomic distance, Å		Lattice ratio, c/a	Hardness, KHN[b]
	a	c		
Hexagonal close packed	[c]3.0817 [d]3.073	[c]15.1183 [d]15.079	[c]4.9058 [d]4.9069	(0001)⟨11$\bar{2}$0⟩, 2917
				(0001)⟨10$\bar{1}$0⟩, 2954
				(10$\bar{1}$0)⟨0001⟩, 2129
				(10$\bar{1}$0) perpendicular ⟨0001⟩, 2755
				(11$\bar{2}$0)⟨0001⟩, 2391
				(11$\bar{2}$0) perpendicular ⟨0001⟩, 2755

[a]Manufacturer's analysis.
[b]Ref. 7.
[c]Ref. 23.
[d]Ref. 24.

Figure 1. - High-vacuum friction and wear apparatus.

Coefficient of friction

(a) 8.12 atomic percent Ti-Fe alloy.

(b) 1.02 atomic percent Ti-Fe alloy.

Number of passes over same track
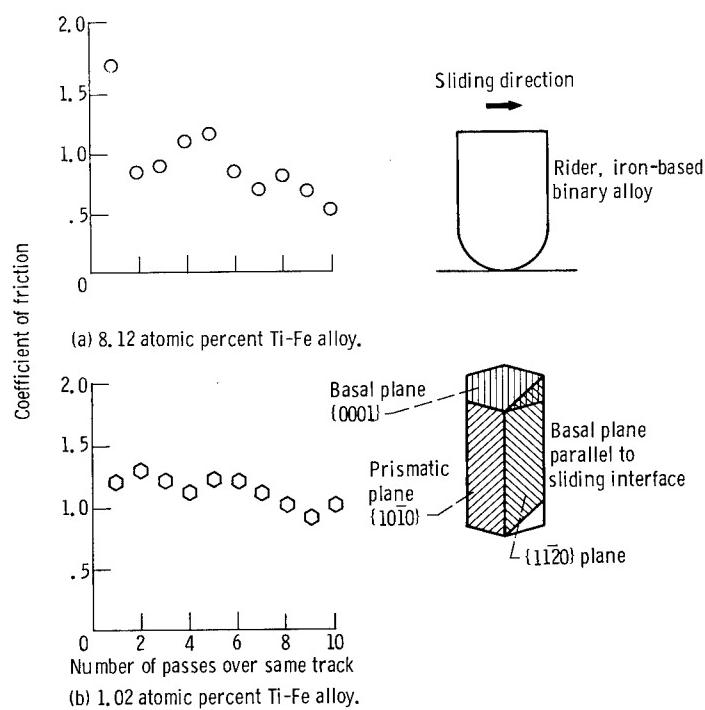
Figure 2. - Coefficient of friction as function of number of passes of alloy riders across single-crystal silicon carbide (0001) surface in high vacuum. Sliding velocity, 3×10^{-3} meter per minute; load, 0.2 newton; room temperature; vacuum, 10^{-8} pascal.

8
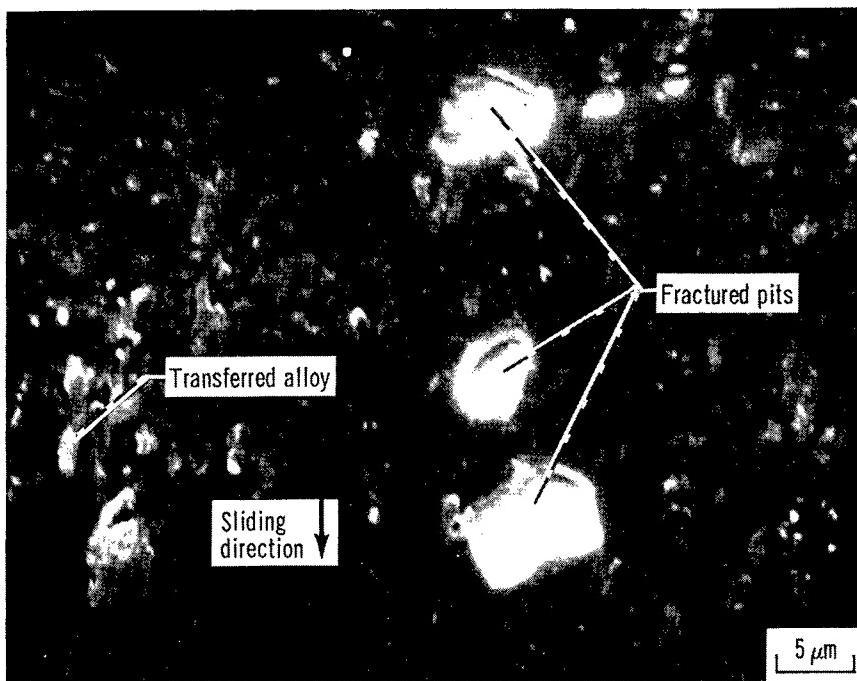
(a) Wear track sliding against 8.06 atomic percent Rh-Fe alloy.
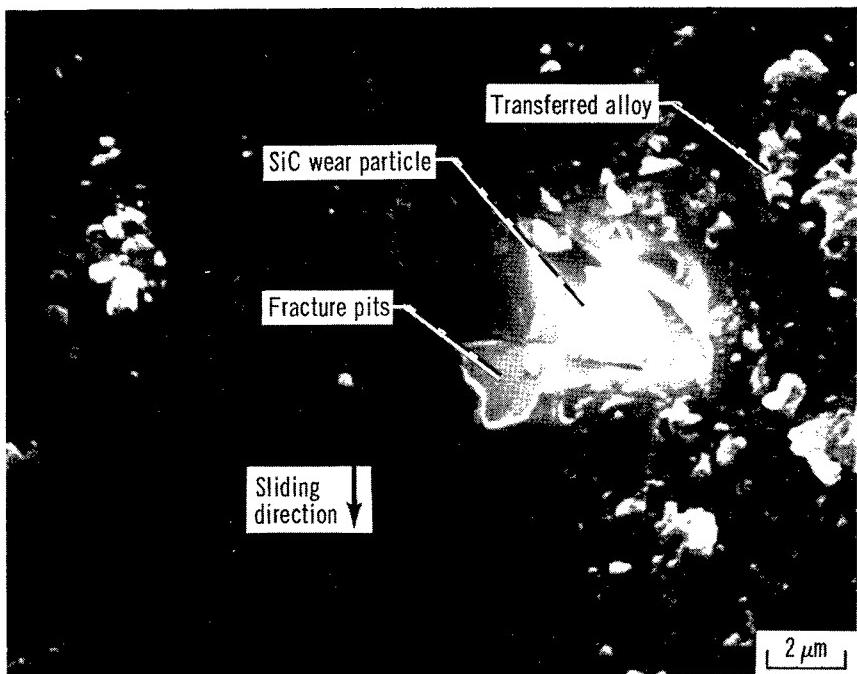
(b) Wear track sliding against 6.66 atomic percent W-Fe alloy.

Figure 3. - Fracture pits of single-crystal silicon carbide in contact with 8.06 atomic percent Rh-Fe alloy, and 6.66 atomic percent W-Fe alloy as results of ten passes of rider in vacuum (10^{-8} Pa). Scanning electron micrographs of wear tracks on silicon carbide (0001) surface. Sliding velocity, 3×10^{-3} meter per minute; load, 0.2 newton; room temperature.

Figure 4. - Large fracture pit of single-crystal silicon carbide in contact with 8.12 atomic percent Ti-Fe alloy as a result of ten passes of rider in vacuum (10^{-8} Pa). A scanning electron micrograph of wear track on silicon carbide (0001) surface. Sliding velocity, 3×10^{-3} meter per minute; load, 0.2 newton; room temperature.
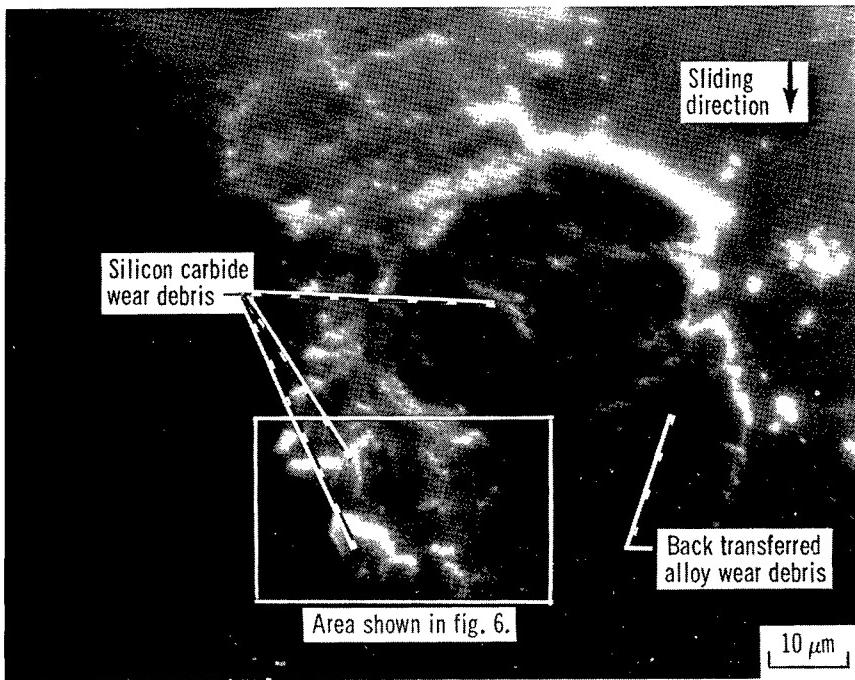
(a) Silicon carbide wear debris.
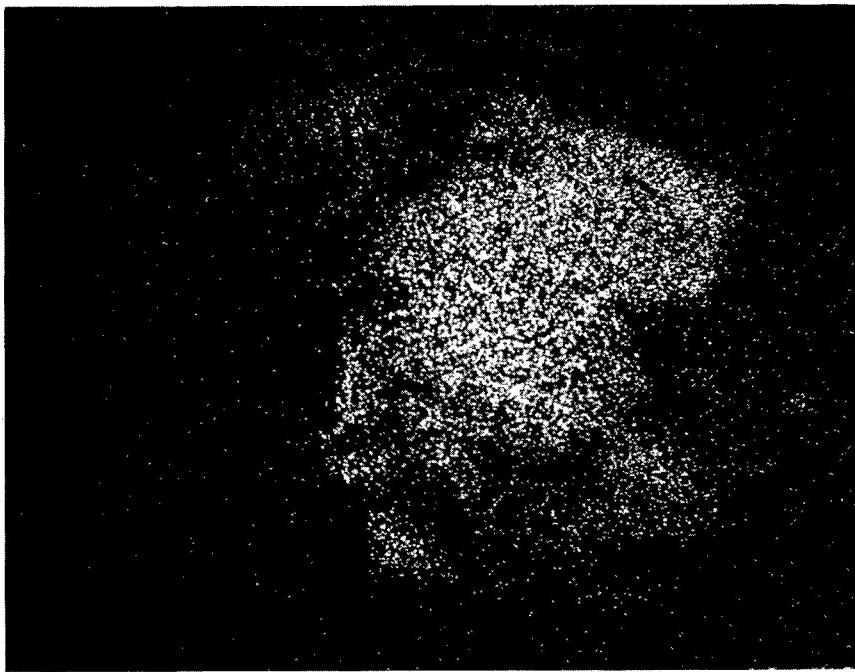
(b) Silicon K_α X-ray map of 8.12 atomic percent Ti-Fe alloy rider; 1×10^4 counts.

Figure 5. - Silicon carbide wear debris on alloy as a result of ten passes of rider in vacuum (10^{-8} Pa). Scanning electron micrograph and an X-ray dispersive analysis of wear scar on alloy rider. Sliding velocity, 3×10^{-3} meter per minute; load, 0.2 newton; room temperature.

11
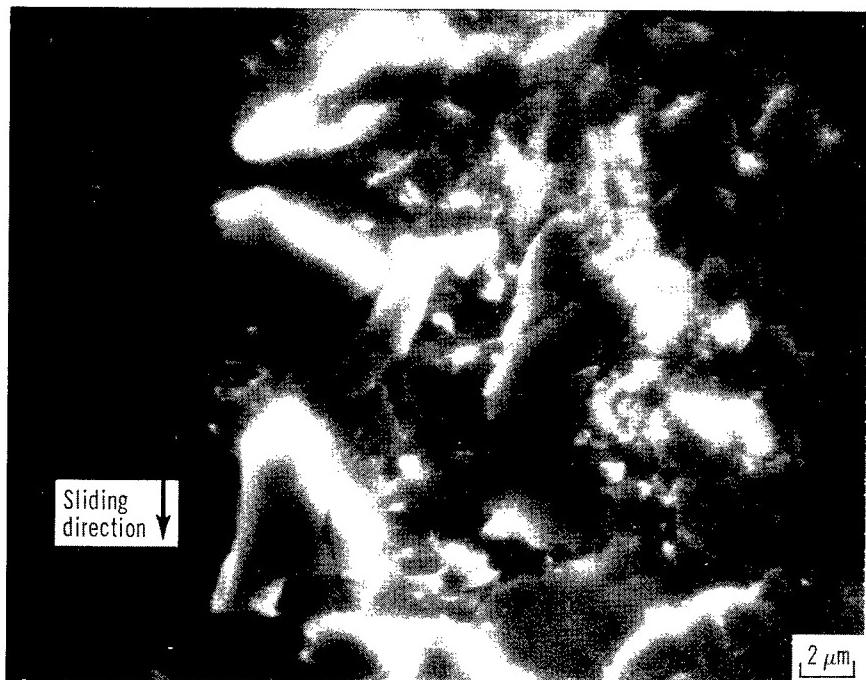
Figure 6. - Silicon carbide wear debris on alloy at high magnification.
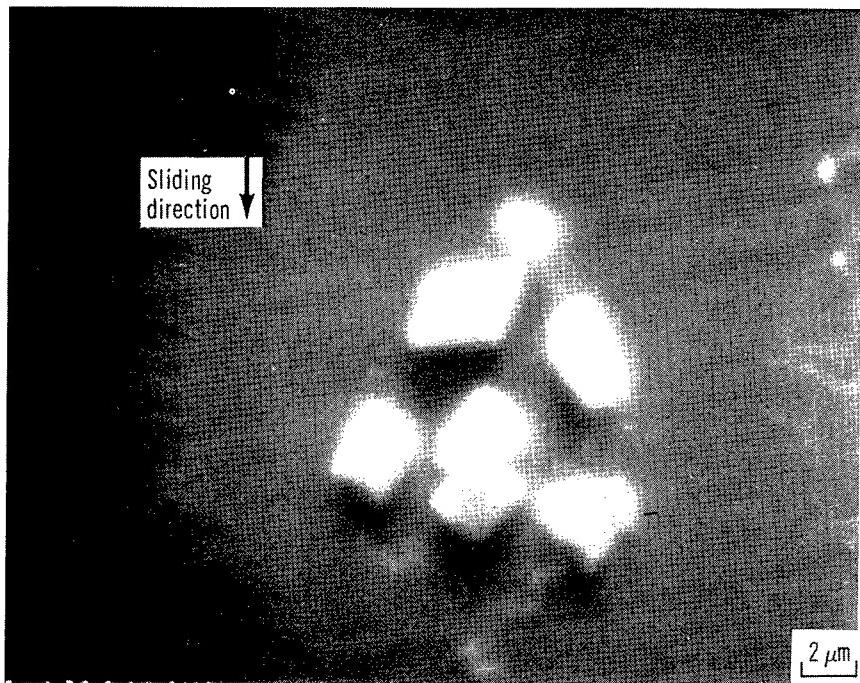
(a) Multiangular wear particle.
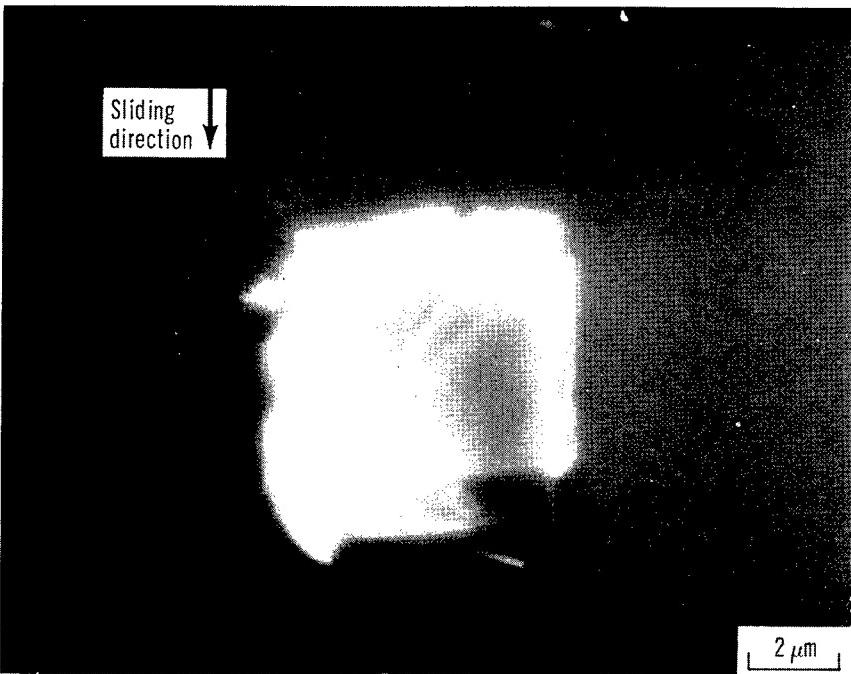
(b) Nearly square-shaped wear particle.

Figure 7. - Multiangular wear debris of single-crystal silicon carbide as result of ten passes of riders in vacuum (10^{-8} Pa); 1.02 atomic percent Ti-Fe alloy slidings and 3.86 atomic percent Ti-Fe alloy slidings. Scanning electron micrographs of wear tracks on disk. Sliding velocity, 3×10^{-3} meter per minute; load, 0.2 newton; room temperature.

13
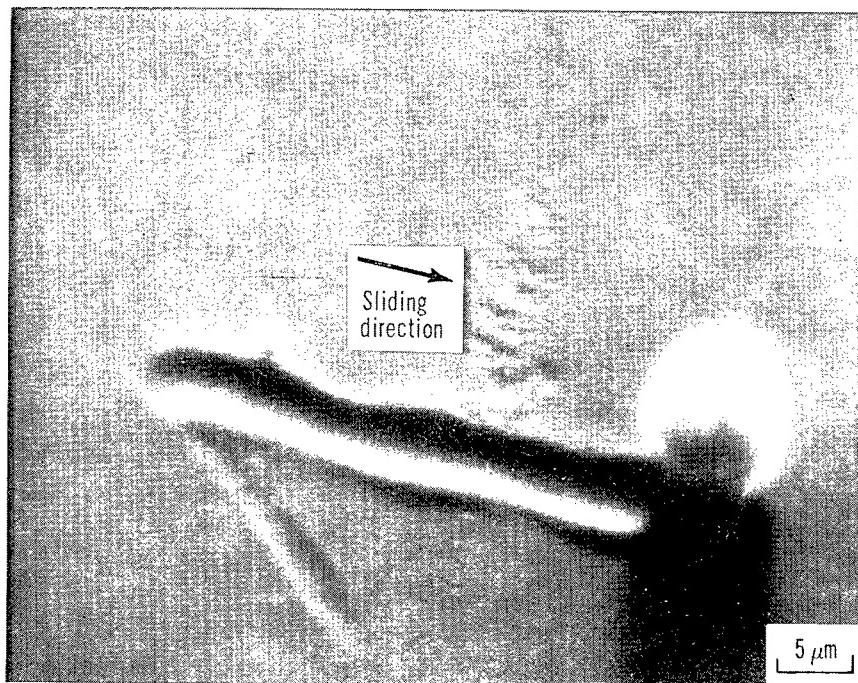
(a) Spherical wear particle and groove.
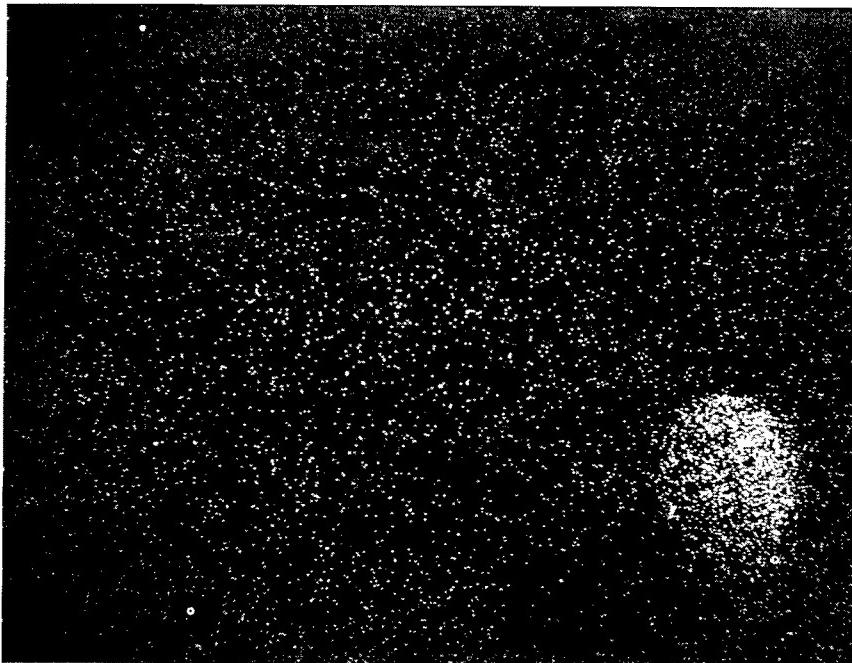
(b) Silicon, K_{α} X-ray map of 1.02 at % Ti-Fe alloy rider; 1×10^4 counts.

Figure 8. - Spherical wear particle on alloy as a result of ten passes of rider in vacuum (10^{-8} Pa). Scanning electron micrograph and an X-ray dispersive analysis of wear scar on alloy rider. Sliding velocity, 3×10^{-3} meter per minute; load, 0.2 newton; room temperature.
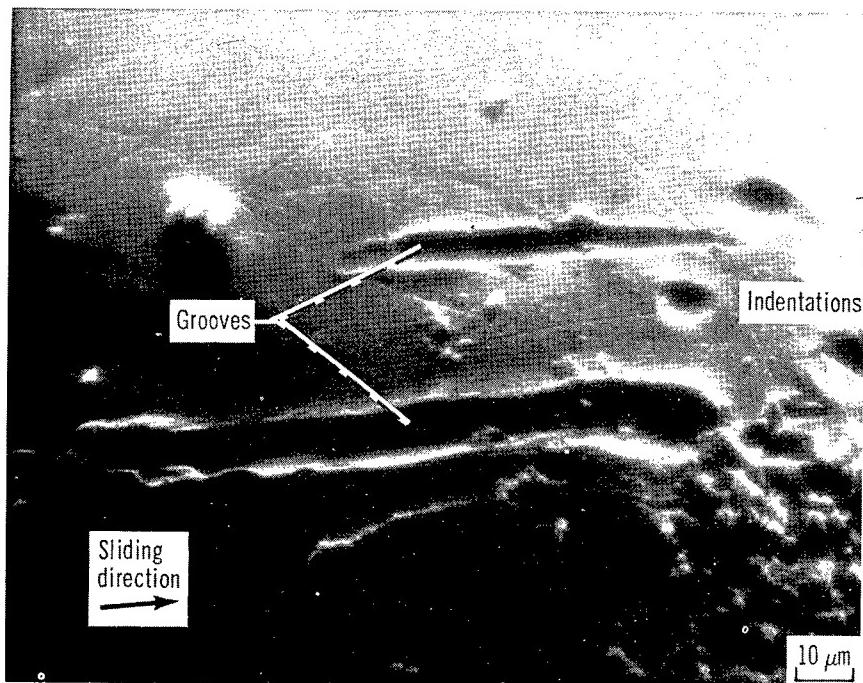
(a) Grooves and spherical indentations.

(b) Groove.

Figure 9. - Grooves and indentations formed by plowing and indenting of spherical wear debris as result of ten passes of rider in vacuum (10^{-8}Pa). Scanning electron micrographs of wear scar on 1.02 atomic percent Ti-Fe alloy rider. Sliding velocity, 3×10^{-3} meter per minute; load, 0.2 newton; room temperature.
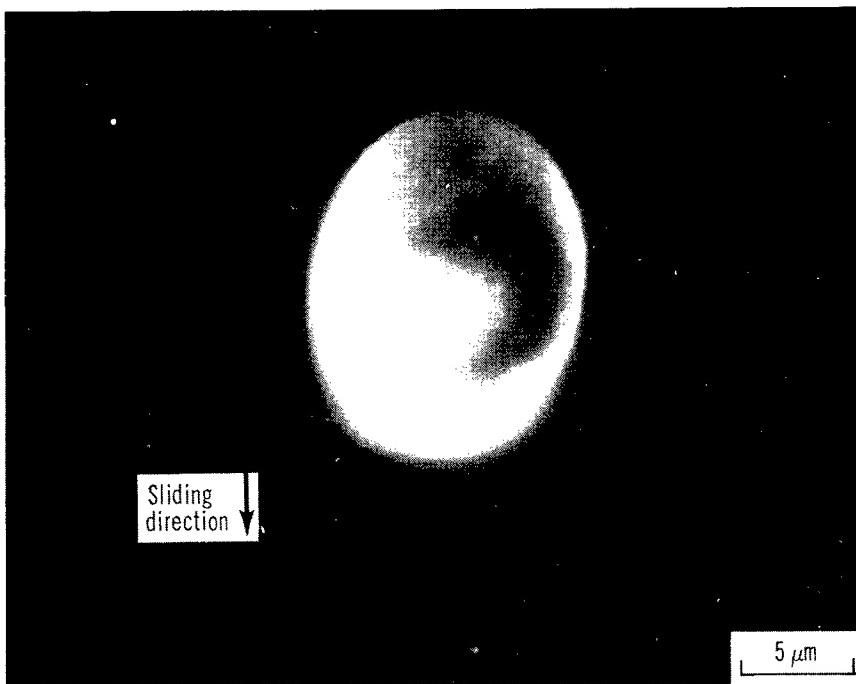
(a) Spherical wear particle.

(b) Spherical and multiangular wear debris.

Figure 10. - Spherical and partially spherical wear particle as result of ten passes of
1.02 atomic percent Ti-Fe alloy riders in vacuum (10^{-8} Pa). Scanning electron micro-
graphs of wear tracks on disk. Sliding velocity, 3×10^{-3} meter per minute; load, 0.2
newton; room temperature.

16
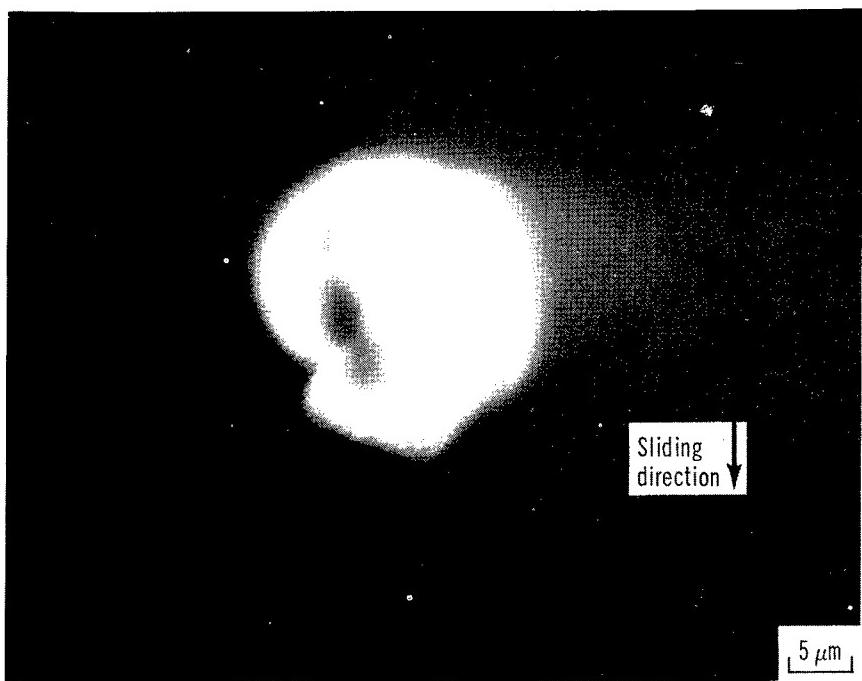
(c) Partially spherical and partially multiangular wear particle.
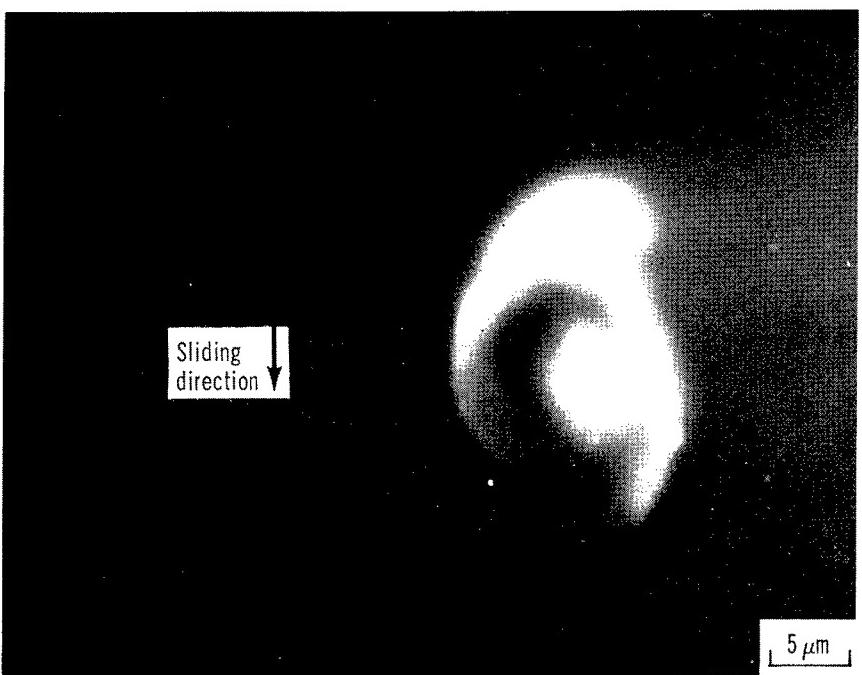
(d) Partially rounded and partially multiangular wear particle.

Figure 10. - Concluded.

17

Figure 11. - Partially spherical wear particle and multiangular wear particles as result of ten passes of 1.02 atomic percent Ti-Fe alloy rider in vacuum (10^{-8} Pa). Scanning electron micrograph of wear scar on alloy rider. Sliding velocity, 3×10^{-3} meter per minute; load, 0.2 newton; room temperature.

18
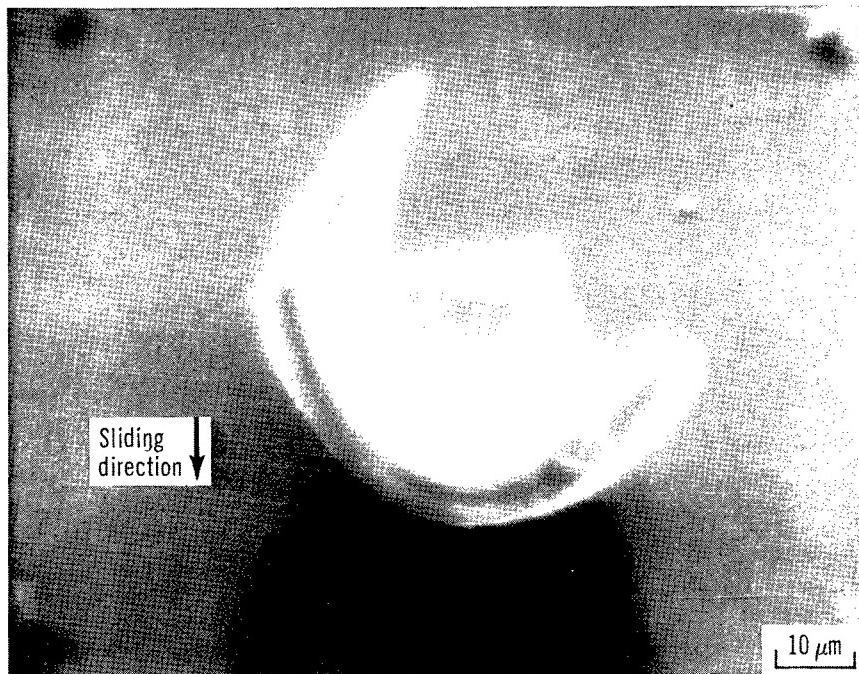
(a) Brittle fractured wear particle with sharp edges.
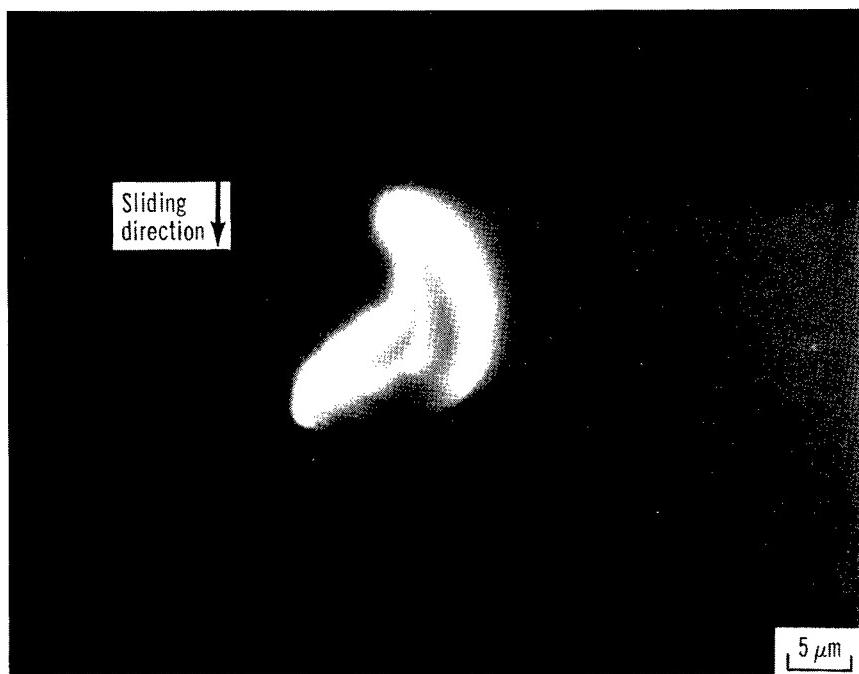
(b) Brittle fractured wear particle.

Figure 12. - Brittle fractured wear particles as result of ten passes of 1.02 atomic percent Ti-Fe alloy rider in vacuum (10^{-8} Pa). Scanning electron micrographs of wear track on disk. Sliding velocity, 3×10^{-3} meter per minute; load, 0.2 newton; room temperature.

19

(a) First stage.

(b) Second stage.

(c) Third stage.

Figure 14. – Schematic of sources of stress concentration under loading and sliding.

$2a_0$: Extent of resulting contact under normal load.

$a_0 + a_1$: Extent of resulting contact under normal load and tangential force

$a_0 + a_2$: Extent of resulting contact under normal load and maximum tangential force.

(a) First stage.

(b) Second stage.

(c) Third stage.

(d) Fourth stage.

(e) Fifth stage.

Figure 13. – Schematic of primary and secondary crack formations under loading and sliding.
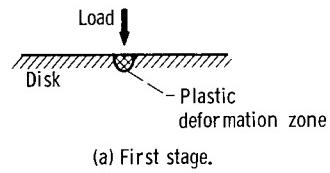
(a) First stage.
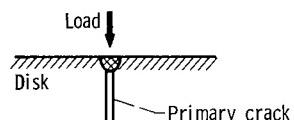
(b) Second stage.
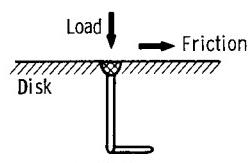
(c) Third stage.
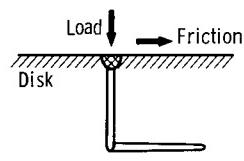
(d) Fourth stage.

Figure 15. - Schematic of crack formation under inelastic deformation zone.
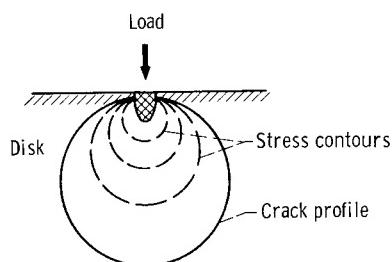
Figure 16. - Schematic of a penny-shaped crack formation under inelastic deformation zone (ref. 22).

1. Report No. NASA TP-1624	2. Government Accession No.	3. Recipient's Catalog No.
4. Title and Subtitle WEAR PARTICLES OF SINGLE-CRYSTAL SILICON CARBIDE IN VACUUM		5. Report Date February 1980
		6. Performing Organization Code
7. Author(s) Kazuhisa Miyoshi and Donald H. Buckley		8. Performing Organization Report No. E-077
9. Performing Organization Name and Address National Aeronautics and Space Administration Lewis Research Center Cleveland, Ohio 44135		10. Work Unit No. 506-16
		11. Contract or Grant No.
12. Sponsoring Agency Name and Address National Aeronautics and Space Administration Washington, D.C. 20546		13. Type of Report and Period Covered Technical Paper
		14. Sponsoring Agency Code

15. Supplementary Notes

16. Abstract

Sliding friction experiments were conducted in vacuum with silicon carbide $\{0001\}$ surface in contact with iron-based binary alloys. Multiangular and spherical wear particles of silicon carbide are observed as a result of multipass sliding. The multiangular particles are produced by primary and secondary cracking of cleavage planes $\{0001\}$, $\{10\bar{1}0\}$, $\{11\bar{2}0\}$ under the Hertzian stress field or local inelastic deformation zone. The spherical particles may be produced by two mechanisms: (1) a penny-shaped fracture along the circular stress trajectories under the local inelastic deformation zone, and (2) attrition of wear particles.

17. Key Words (Suggested by Author(s)) Spherical wear particle Fracture Ultrahigh vacuum Alloys Silicon carbide		18. Distribution Statement Unclassified – unlimited STAR Category 27	
19. Security Classif. (of this report) Unclassified	20. Security Classif. (of this page) Unclassified	21. No. of Pages 23	22. Price* A02